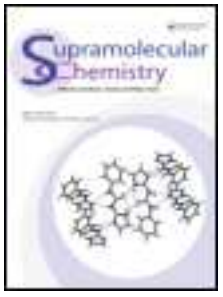

Supramolecular Chemistry
Publication details, including instructions for authors and subscription information:
http://www.tandfonline.com/loi/gsch20

Self-assembly snapshots of a 2 × 2 copper(I) grid

Lauren E. Manck[a], Christopher R. Benson[b], Andrew I. Share[b], Hyunsoo Park[b], Douglas A. Vander Griend[a] & Amar H. Flood[b]

[a] Department of Chemistry & Biochemistry, Calvin College, Grand Rapids, MI49546-4403, USA

[b] Department of Chemistry, Indiana University, 800 E. Kirkwood Avenue, Bloomington, IN47405, USA

Published online: 14 Feb 2014.

To cite this article: Lauren E. Manck, Christopher R. Benson, Andrew I. Share, Hyunsoo Park, Douglas A. Vander Griend & Amar H. Flood , Supramolecular Chemistry (2014): Self-assembly snapshots of a 2 × 2 copper(I) grid, Supramolecular Chemistry, DOI: 10.1080/10610278.2013.872780

To link to this article: http://dx.doi.org/10.1080/10610278.2013.872780

Supramolecular Chemistry, 2014
http://dx.doi.org/10.1080/10610278.2013.872780

Self-assembly snapshots of a 2 × 2 copper(I) grid

Lauren E. Manck[a], Christopher R. Benson[b], Andrew I. Share[b], Hyunsoo Park[b], Douglas A. Vander Griend[a]* and Amar H. Flood[b]*

[a]*Department of Chemistry & Biochemistry, Calvin College, Grand Rapids, MI 49546-4403, USA;* [b]*Department of Chemistry, Indiana University, 800 E. Kirkwood Avenue, Bloomington, IN 47405, USA*

(*Received 22 July 2013; accepted 3 December 2013*)

Self-assembled 2 × 2 grids have been characterised as high-fidelity species produced when the correct stoichiometric ratios are met, but rarely are the individual steps leading to and from their formation characterised. Here, we present such a study using equilibrium-restricted factor analysis to model a set of UV–vis spectra starting from a bis-bidentate ligand to the assembly of a 2 × 2 grid complex upon titration with 1 equiv. of $[Cu(MeCN)_4](PF_6)$ and to disassembly upon further titration. Intermediate species $[Cu\mathbf{L}_2]^+$, $[Cu_2\mathbf{L}_3]^{2+}$, $[Cu_3\mathbf{L}_2]^{3+}$ and $[Cu_2\mathbf{L}]^{2+}$ are evidenced along the assembly and disassembly pathways. Complementary ^{1}H NMR titrations are consistent with the rich set of complexes and equilibria involved. Given the nature of the assembly process, the assembly is entropy driven and likely enthalpy driven as well. The disassembly process is both enthalpy and entropy driven according to the standard free energy values derived from the modelling of the spectrophotometric titration data.

Keywords: grid complexes; self-assembly; metal–ligand bonding; NMR; spectrophotometric titration

Introduction

As technological innovations continue to move towards materials that demand regularly ordered nanometre-sized features (*1*), non-covalent syntheses (*2*) that can realise self-assembled supramolecular structures from smaller building blocks are required. With increasing frequency, this 'bottom up' method of production has been utilised (*3*). Thus, the role of supramolecular chemistry has grown in prominence through the burgeoning field of nanotechnology (*4*) where the preparation of a wide range of discrete and high-fidelity assemblies is well documented (*5*, *6*). The basis of supramolecular chemistry is the spontaneous assembly of non-covalently linked molecular clusters (*7*) designed to yield thermodynamically favoured structures. As excellent examples, Levin and Stang have demonstrated the formation of a supramolecular dodecahedron from the coming together of 50 molecules of two different types (*8*). However, as the complexity of these supramolecular structures increases, the possibility for alternate arrangements that lower the fidelity or alter the stoichiometry of the multicomponent assembly also increases. For instance, Long et al. have shown that the preference of a ruthenium(II) complex to form either a square or a triangular supramolecule depends on the surrounding solvent (*9*). In order to most effectively access the potential offered by various nanoscale structures and to apply rational design (*10*) in the non-covalent synthesis (*2*) of novel structures, a greater level of detail in the characterisation of the assembly process (*11*) is necessary for facilitating a deeper understanding.

Included amongst the possible self-assembled structures are squares (*12*), grids (*13*), racks (*14*) and ladders (*15*) that are expressed within homogeneous solutions in two dimensions with many other assemblies (*16*) also present in one (*17*) and three (*10*, *15*) dimensions. The 2 × 2 grids composed of four metal ions, (two in the *x*-axis and two in the *y*) combined with four ligands constitute some of the earliest (*13*) examples. These grids are also of sufficient complexity to serve as exemplary species for experimental interrogation and as complements to theoretical approaches (*18*) prior to the evaluation of larger assemblies. When these self-organising structures can be realised with easy-to-synthesise ligands, opportunities exist for other materials to be fashioned from them. With these ideas in mind, we present a detailed thermodynamic study of a 2 × 2 grid that employs a click-derived ligand, **L** = 3,6-bis(1-(2-(2-(2-methoxyethoxy)ethoxy)ethyl)-1H-1,2,3-triazol-4-yl)pyridazine (Figure 1(a)). Supramolecular coordination complexes derived from click ligands have become a familiar sight in the literature in the last few years (*19*), with Crowley (*20*), Ward (*21*), Policar (*22*) and Petitjean (*23*) as exemplars. A similar grid motif was recently reported (*24*) by Schubert during the preparation of our study based on the same 3,6-bis(1,2,3-triazol-4-yl)pyridazine core. Schubert confirmed using NMR and high-resolution ESI-TOF mass spectrometry that the 2 × 2 grid was formed at a 1:1 ratio of ligand to Cu(I); however, the assembly process itself was not determined. In fact, characterisation of these

*Corresponding authors. Email: dvg@calvin.edu; aflood@indiana.edu

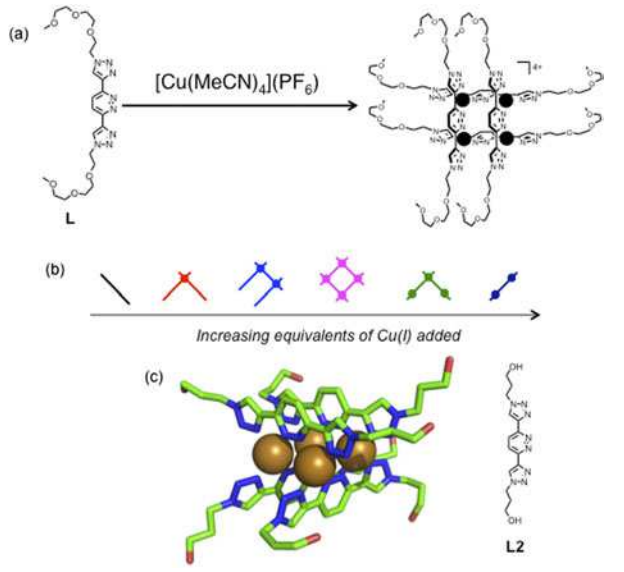

Figure 1. (Colour online) (a) Representation of the formation of the grid complex from the bis-bidentate ligand (**L**) and (b) the progression of dominant species involved in the self-assembly of the 2 × 2 grid between **L** and Cu(I) during the titration of metal cations into ligand. (c) Crystal structure of the 2 × 2 grid with PF_6^- counteranion (not shown) formed with **L2**.

multiple component assemblies using titrations are rare (*24*) and are generally non-trivial to analyse (*13*). Thus, we provide a critical look into the inner workings of a 2 × 2 grid to help deepen the understanding in this area of supramolecular chemistry (*25*).

Equilibrium-restricted factor analysis (ERFA) [26] is employed initially to characterise the stepwise assembly of the grid. ERFA is a form of principle component analysis that requires the components along the compositional axis to adhere to the strictures of equilibrium mixtures. It allows thermodynamic quantities to be obtained via optimisation while multiple species remain in an equilibrium mixture, and it can give great insight into the assembly process of various supramolecular structures. ERFA is implemented here using the computer program SIVVU™ (*26*). The number of distinct absorbing species, their individual spectroscopic signatures and the free energy values for the chemical reactions between them are ascertained from UV–vis absorption data collected from a series of solutions of varying compositions (*6*, *27*). This approach has already been used successfully to interrogate the step-wise formation of a tetrahedron derived from six ligands and four cobalt(II) ions (*11*). The formation of two-dimensional supramolecular grids under investigation here takes advantage of the tetrahedral coordination of copper(I) with a bis-bidentate ligand in dichloromethane. A crystal structure was generated (Figure 1(c)), and although the crystal showed weak diffraction, it confirmed unambiguously the connectivity expected for the grid. Using a quantitative thermodynamic analysis of the assembly process (Figure 1(b)), five equilibria were identified that span from the free ligand through two pre-grid intermediates, the grid itself and then through two more post-grid complexes. Corroborating evidence for some of the species predicted in the ERFA model of the UV–vis spectrophotometric titration was examined utilising electrospray ionisation mass spectrometry (ESI-MS). The number of equilibria was found to be consistent with ^{1}H NMR titrations conducted at various temperatures. The analysis shows that the thermodynamic intermediates of assembly (in which the stoichiometric ratio of Cu:L is not the ideal 1:1 required for the grid) maximise the number of metal–ligand coordinative bonds while spreading the positive charges of the copper cations as much as possible. Overall, we conclude that the assembly and subsequent disassembly of the supramolecular grid is entropy driven in dichloromethane (CH_2Cl_2) solution.

Methods

ERFA modelling of UV–vis by titration

In order to determine the thermodynamic properties of this system, the absorbance data was modelled using ERFA with the computer program SIVVU™ (*28*). SIVVU™ has shown itself to be a valuable tool in the determination of both binding constants and dissection of both organic (*29*) and inorganic (*30*) complexes. Absorbance and composition data were input into the program. The additive structure of the former is analysed initially in order to determine the number of unique absorbers that contribute to the data. Then, the entire dataset is modelled under the constraints of chemical equilibrium and Beer's law. The ΔG values corresponding to chemical reactions provided by the user were optimised to achieve the smallest deviation between the measured and calculated absorbance values, and in the process, concentration and molar absorptivity values for each of the absorbing chemical species were determined (*27*, *31*). The concentrations need to be sufficiently dilute to allow a reasonable population of both products and reactants. When this criterion is fulfilled, the accuracy of the ΔG values is high (*26*, *32*).

Results and discussion

X-ray crystallography of the $[Cu_4(L2)_4](PF_6)_4$ complex

The connectivity of a grid complex based on the ligand **L2** (Figure 1(c)) was confirmed by the crystal structure obtained from synchrotron single crystal X-ray diffraction data. As expected, the typical grid structure (*13*) is obtained with all bidentate binding sites fulfilled on the ligand with four-coordinate copper(I) geometries and the ligand pairs π-stacked. The crystals of $[Cu_4(\mathbf{L2})_4](PF_6)_4$ were extremely small (approximate dimensions 0.07

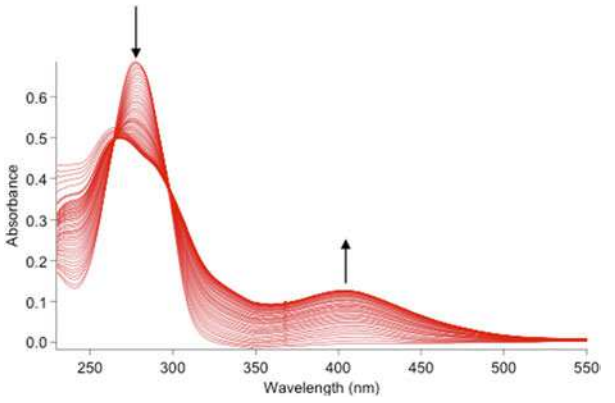

Figure 2. (Colour online) Total set of absorbance data used in the equilibrium-restricted factor analysis. Fifty solutions of **L** (20 μM, dichloromethane) with 0–2.14 equiv. of copper(I).

$\times 0.07 \times 0.01\,mm^3$) and weakly diffracting. The diffraction data were acquired with synchrotron X-ray radiation at ChemMatCARS beamline, Advanced Photon Source, Argonne National Laboratory. Despite the use of synchrotron radiation, the crystal diffracted very poorly, and the quality of data was not sufficient enough to refine the details of the structure such as anisotropic thermal parameters. Nevertheless, the connectivity of the $[Cu_4(\mathbf{L2})_4](PF_6)_4$ complex could be established straightforwardly. As such, while the technical parameters for the crystal are poor, the principal finding (and our rationale for including the structure) was to confirm the connectivity of the complex, and this result is verifiable.

UV–vis titration and quantitative analysis

The titration of **L** with 2 equiv. of copper(I) in dichloromethane yielded consistently varying absorbance data (Figure 2). This titration was characterised by an intense peak at 278 nm which diminished and shifted to 265 nm while a broader peak at 400 nm grew in. A factor analysis that is not restricted by the chemical equilibria was used to independently identify the number of absorbing species (Table 1) indicating that there are at least five additive factors (i.e. absorbers) that comprise 99.28% of the information within the entire absorbance dataset of 50 solutions across the wavelength range 230–550 nm. A cut-off at the fifth absorber was based on the fact that it is the last factor with a weighting (0.0652) that is more than twice that of the weightings for the subsequent sixth factor (0.0285). The unrestricted factor analysis suggests that a sixth, seventh and even eighth absorber still remain possibilities on account of the fact that these values are still noticeably larger, although not twice the magnitude of subsequent values. Upon testing scores of potentially reasonable models, the best model was obtained with a total of seven absorbers, corresponding to the uncomplexed ligand, **L** and uncomplexed copper ion, both being the species added to the solution. Next, are two pre-grid complexes $[CuL_2]^+$ and $[Cu_2L_3]^{2+}$ followed by the grid complex $[Cu_4L_4]^{4+}$ and then there are two post-grid complexes $[Cu_3L_2]^{3+}$ and $[Cu_2L]^{2+}$.

Table 1. Breakdown and ranking of additive factors in UV–vis absorbance data.

Unrestricted factor	Factor weight	Cumulative percentage (%)
1	41.9763	83.95
2	6.5579	97.07
3	0.7170	98.50
4	0.3255	99.15
5	0.0652	99.28
6	0.0285	99.34
7	0.0190	99.38
8	0.0161	99.41
9	0.0139	99.44
10	0.0136	99.47

These absorbers were modelled using equilibria that were constructed by employing coefficients (1/2, 3/2, 3/8, 1/4) to standardise each reaction to the addition of half a copper cation. This standard is equal to the formation of a single metal–ligand linkage through two metal–nitrogen coordinative bonds.

All of the absorbance data from 230 to 550 nm for all 50 solutions could be accurately modelled using equilibria 1–5.

$$\frac{1}{2}[Cu(MeCN)_4]^+ + \mathbf{L} \rightleftharpoons \frac{1}{2}[CuL_2]^+ + 2\,MeCN, \quad (1)$$

$$\frac{1}{2}[Cu(MeCN)_4]^+ + \frac{3}{2}[CuL_2]^+ \rightleftharpoons [Cu_2L_3]^{2+} + 2\,MeCN, \quad (2)$$

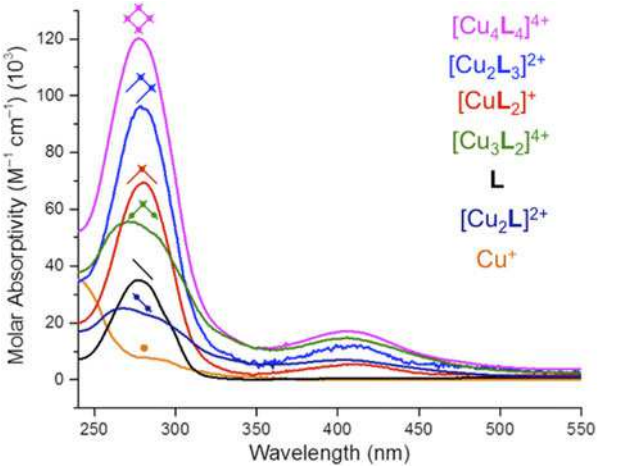

Figure 3. (Colour online) Molar absorptivity values for the seven absorbing species present in the series of solutions as determined by equilibrium-restricted factor analysis.

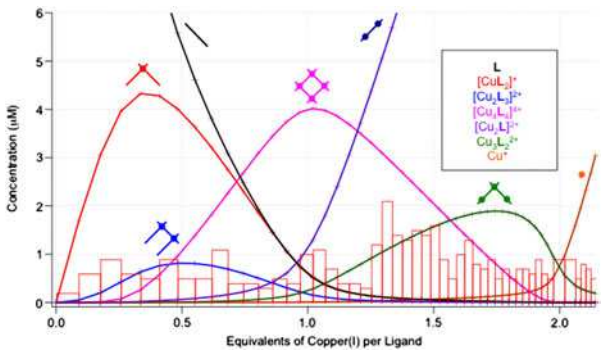

Figure 4. (Colour online) Concentration profiles for the 50 solutions with **L** and copper(I). Bars represent the root mean square residual for each solution in the ERFA model.

$$\frac{1}{2}[\mathrm{Cu(MeCN)_4}]^{+} + \frac{1}{2}[\mathrm{Cu_2L_3}]^{2+} \rightleftharpoons [\mathrm{Cu_4L_4}]^{4+} + 2\ \mathrm{MeCN}, \quad (3)$$

$$\frac{1}{2}[\mathrm{Cu(MeCN)_4}]^{+} + \frac{1}{4}[\mathrm{Cu_4L_4}]^{4+} \rightleftharpoons \frac{1}{2}[\mathrm{Cu_3L_2(MeCN)_4}]^{3+}, \quad (4)$$

$$\frac{1}{2}[\mathrm{Cu(MeCN)_4}]^{+} + \frac{1}{2}[\mathrm{Cu_3L_2}]^{3+} \rightleftharpoons [\mathrm{Cu_2L(MeCN)_4}]^{2+}, \quad (5)$$

The final R^2 for the fit was 99.9973% with a root mean square residual of 0.00087. None of the alternative models investigated were acceptable. The model yielded molar absorptivity curves for each of the seven absorbers (Figure 3) and concentration profiles for each species throughout the titration (Figure 4). It should be noted that unbound acetonitrile does not absorb in the range of wavelengths studied, and therefore, it is not possible to explicitly include it as a participant in the model for the purposes of the SIVVU™ analysis. The NMR titration (3 mM) shows the acetonitrile getting ejected as expected during the first three equilibria steps (Table 2) indicating that its affinity for copper(I) is weak compared to that of the ligand. The concentration profiles (Figure 4) show the consumption of **L**, the gradual formation and loss of each of the five complexes and the excess copper(I) at the end of the titration. The 1:2 pregrid $[\mathrm{CuL_2}]^{+}$, the 4:4 grid $[\mathrm{Cu_4L_4}]^{4+}$ and the 2:1 post-grid $[\mathrm{Cu_2L}]^{2+}$ complexes were formed in the highest concentrations with the 2:3 pre-grid and 3:2 post-grid complexes, $[\mathrm{Cu_2L_3}]^{2+}$ and $[\mathrm{Cu_3L_2}]^{3+}$, respectively, being formed in smaller concentrations. The concentration profile shows that the $[\mathrm{Cu_4L_4}]^{4+}$ grid is the dominant, but not only, complex formed in solution at 1 equiv. of Cu(I) added. As expected, beyond 2 equiv. of Cu(I), the concentration of the uncomplexed metal cation increases substantially.

From the first complex to the last, the UV peak positions progressively blue shift: 280, 279, 277, 271, then 267 nm with molar absorptivity values on a *per ligand basis* of 3.47×10^4, 3.21×10^4, 3.00×10^4, 2.78×10^4 and $2.52 \times 10^4\ \mathrm{M^{-1}\,cm^{-1}}$, respectively. Under these equilibrium-restricted constraints, these molar absorptivity spectra, along with the curves for free ligand and the copper(I) *solvato* complex, account for 99.21% of the data set that was collected. The free energy values for the formation of each of the reactions in Table 2 at 295 K were likewise refined. The overall root-mean-square residual for this optimisation was 0.00087 with the error associated

Table 2. Standard free energy values for the successive addition of Cu(I) to form each $[\mathrm{Cu}_x\mathbf{L}_y]^{x+}$ complex.

Complex formation reaction	ΔG° (kJ mol^{-1})	log (K)
$\frac{1}{2}\mathrm{Cu}^{+} + \mathbf{L} \rightleftharpoons \frac{1}{2}[\mathrm{CuL_2}]^{+} + 2\,\mathrm{MeCN}$	−40.5(6)	7.17
$\frac{1}{2}\mathrm{Cu}^{+} + 1\frac{1}{2}[\mathrm{CuL_2}]^{+} \rightleftharpoons [\mathrm{Cu_2L_3}]^{2+} + 2\,\mathrm{MeCN}$	−37(2)	6.55
$\frac{1}{2}\mathrm{Cu}^{+} + \frac{1}{2}[\mathrm{Cu_2L_3}]^{2+} \rightleftharpoons \frac{3}{3}[\mathrm{Cu_4L_4}]^{4+} + 2\,\mathrm{MeCN}$	−31(2)	5.49
$\frac{1}{2}\mathrm{Cu}^{+} + \frac{1}{4}[\mathrm{Cu_4L_4}]^{4+} \rightleftharpoons \frac{1}{2}[\mathrm{Cu_3L_2(MeCN)_4}]^{3+}$	−11.9(2)	2.11
$\frac{1}{2}\mathrm{Cu}^{+} + \frac{1}{2}[\mathrm{Cu_3L_2}]^{3+} \rightleftharpoons [\mathrm{Cu_2L(MeCN)_4}]^{2+}$	−8.0(2)	1.42

with each solution shown as bars below the concentration profiles (Figure 4).

Use of ERFA has afforded a model for the step-wise assembly and disassembly of the self-assembling 2 × 2 copper(I) grid $[Cu_4\mathbf{L}_4]^{4+}$ in dichloromethane. Five distinct complexes are identified in solution throughout the addition of a little over 2 equiv. of copper(I) to the ligand, and this approach allows for the characterisation of each species without the necessity of their isolation. This outcome is not only convenient when facing the challenge of isolation but more importantly, this strategy allowed the interplay between complexes to be explored as the grid comes together and falls apart in solution.

The presence of five complexes $[Cu\mathbf{L}_2]^{+}$, $[Cu_2\mathbf{L}_3]^{2+}$, $[Cu_4\mathbf{L}_4]^{4+}$, $[Cu_3\mathbf{L}_2]^{3+}$ and $[Cu_2\mathbf{L}]^{2+}$ (Figure 1(b)) in addition to the copper(I) *solvato* complex and uncomplexed ligand is consistent with the mathematical structure of the absorbance data which showed that at least five additive factors comprised the data set with a possibility for a sixth and seventh. In the final model, seven purely mathematical (unrestricted) factors accounted for 99.38% of the data, and when the model must conform to the constraints of chemical equilibrium, it still accounts for 99.21% of the measured absorbance data. This strongly indicates that the model is complete and accurate.

The resulting molar absorptivity curves associated with each species (Figure 3) for this model are sensible. Each of the UV bands is in a range that is consistent with the expected intensity for ligand-centred (LC) transitions. The molar absorptivity values for the peaks increase as the number of ligands in the complex increase up to the grid and then decrease as the number of ligands in the complexes decrease. These LC bands also show a consistent shift from 280 to 268 nm as the ligand becomes saturated with copper(I) and they become broader beyond the grid. These features enhance the legitimacy of the model on account of the fact that the mathematical modelling of the data does not take any *a priori* spectroscopic information into account.

Furthermore, the metal-to-ligand charge-transfer (MLCT) band near 400 nm shows a consistent intensity profile across each of the five complexes. Each metal–ligand bidentate site represents an opportunity for an MLCT transition. Thus, the five complexes are expected to have two, four, eight, four and two such opportunities, and the respective molar absorptivity values at 400 nm for each species (0.55×10^4, 1.2×10^4, 1.7×10^4, 1.4×10^4 and 0.7×10^4 ABS/M/cm) reflect this prediction (Figure 3). The peak position also shifts monotonically from 410 nm for $[Cu\mathbf{L}_2]^{+}$ to 403 nm for $[Cu_2\mathbf{L}]^{2+}$.

The 2:3 $[Cu_2\mathbf{L}_3]^{2+}$ pre-grid complex is formed in the lowest concentration (Figure 4) of any of the complexes, which predicated our evaluation of its importance to the data fitting. Without it, the root mean square residual only increases by less than 1%. However, when included, its molar absorptivity curve is consistent with the rest of the complexes and this is strong evidence for its existence. The inclusion of a truly spurious species in a model tends to lead to molar absorptivity curves that have no chemical explanation as they are being used by the model to account for signal noise. Consequently, its inclusion is merited in the model. The removal of both the pre-grid $[Cu_2\mathbf{L}_3]^{2+}$and the post-grid $[Cu_3\mathbf{L}_2]^{3+}$ complexes from the model resulting in a total of five absorbing factors (the minimum number of mathematical factors) increases the root mean square residual from 0.00087 to 0.0013 and results in a nonsensical molar absorptivity curve for the 2 × 2 grid, which is now formed in insignificant amounts. Given these results, the best model was determined to be the one which included both $[Cu_2\mathbf{L}_3]^{2+}$ and $[Cu_3\mathbf{L}_2]^{3+}$ for a total of seven factors.

Electrospray mass spectrometry

While ERFA is a powerful tool for identifying distinct absorbers in solution, it works especially well with species that do not have the same empirical formula. If species do have the same empirical formula, e.g. $[Cu_2\mathbf{L}]^{2+}$ and $[Cu_4\mathbf{L}_2]^{4+}$ then it can be very difficult (though not impossible) to resolve them on a compositional basis.

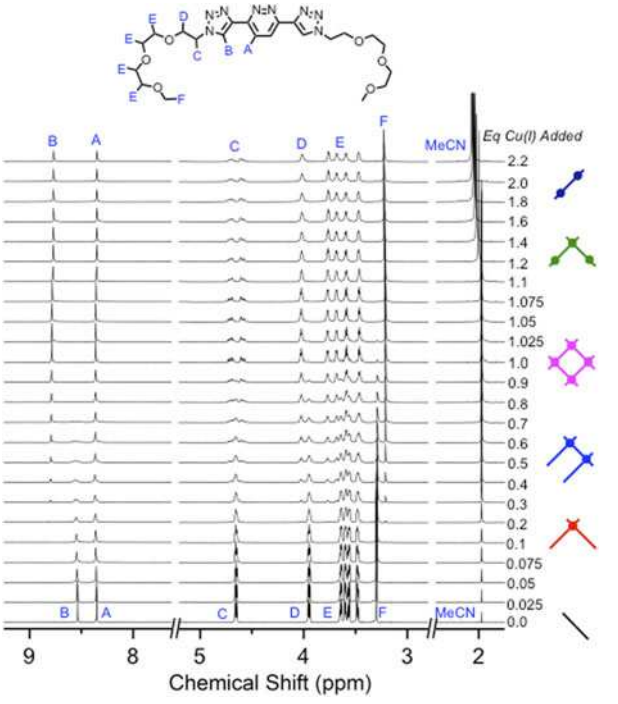

Figure 5. (Colour online) NMR titration of **L** with increasing equivalents of Cu(I) (3 mM **L**, $[Cu(MeCN)_4](PF_6)$ in CD_2Cl_2, 500 MHz, 300 K).

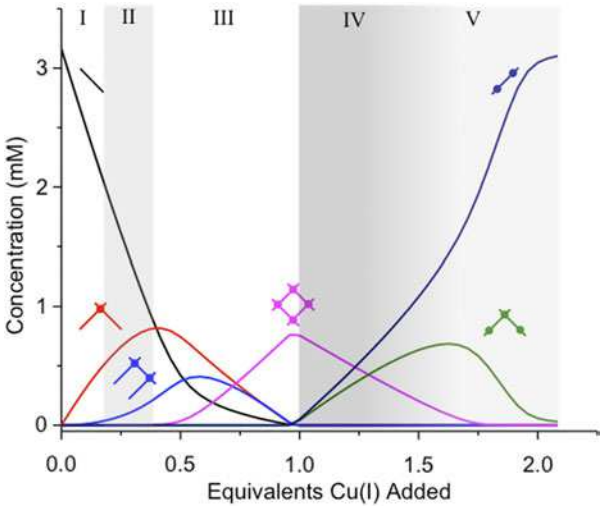

Figure 6. (Colour online) Speciation curve for a 3-mM titration calculated from the SIVVU model generated from the UV–vis titration. Alternating shaded/unshaded regions reflect five different phases observed in the titration.

For this reason, mass spectrometry is an excellent complement to ERFA as a tool that can identify the exact molecular size of the different chemical species.

An ESI-MS titration was conducted to identify the presence of complexes. Only monocationic species were observed, presumably the results of facile complex reductions in the electrospray experiment. All stages of the titration showed the presence of small structures with low copper saturation, e.g. **L**, $[Cu\mathbf{L}_2]^+$ and $[Cu\mathbf{L}]^+$ indicative of fragmentation from larger species. These species remain abundant throughout the titration. Beyond 1 equiv., evidence for species of higher nuclearity develops in the form of $[Cu_2\mathbf{L}_2]^{2+}$ as a minor species. Peaks assigned to $[Cu_2\mathbf{L}]^{2+}$ also appeared intermittently throughout the titration. The presence of moderately saturated copper complexes up to 1 equiv. and highly saturated complexes beyond 1 equiv. support the proposed model.

^{1}H NMR titration

To support the set of equilibria proposed using the analysis of UV–vis titration, an NMR study (Figure 5) characterising the production and loss of the $[Cu_4\mathbf{L}_4]^{4+}$ species and the transitional intermediates (Figure 10) was conducted. A 3-mM solution of **L** was prepared in CD_2Cl_2 to which Cu(I) was added in partial equivalents as the $[Cu(MeCN)_4](PF_6)$ salt. Given the high concentration, it is anticipated that this titration would be occurring under tight-binding conditions. On the basis of related Cu(I) complexes of polyazine ligands (*13*, *33*), the evolution of peaks throughout the titration is expected to reflect a process of slow chemical exchange on the NMR time scale. Overall, our results support the richness and complexity in the numbers of equilibria proposed in the SIVVU™ analysis.

New speciation curves were generated (Figure 6) for the NMR experiment using the parameters determined through the SIVVU™ analysis. The *evolution* of species in the NMR titration is similar to the UV–vis titration. For example, the $[Cu_4\mathbf{L}_4]^{4+}$ grid still represents the dominant species in solution at 1 equiv. General features of the ^{1}H NMR titration (Figure 5) agree with the predictions made in the speciation curve. The growth and loss of key proton resonances (H^B, H^E and H^F) are diagnostic and ultimately allowed identification of five phases of behaviour (see marked regions in Figure 6).

Beginning with the clearest observations, the emergence of a break at a 1:1 molar ratio is seen in the acetonitrile methyl peaks that originate from the copper(I) salt $[Cu(MeCN)_4](PF_6)$. During the addition of up to 1 equiv., all the copper will bind to the available ligands, liberating acetonitrile into solution. At 1 equiv., each copper ion will be saturated with ligands, but beyond it, the copper ions will have vacant sites available for solvation. Consequently, any acetonitrile molecules should be able to form complexes during this latter phase of the titration. Our results reflect this expected behaviour. This peak grows in intensity (Figure 7(b)) as more $[Cu(MeCN)_4](PF_6)$ salt is added. The acetonitrile peak starts at ~1.95 ppm,

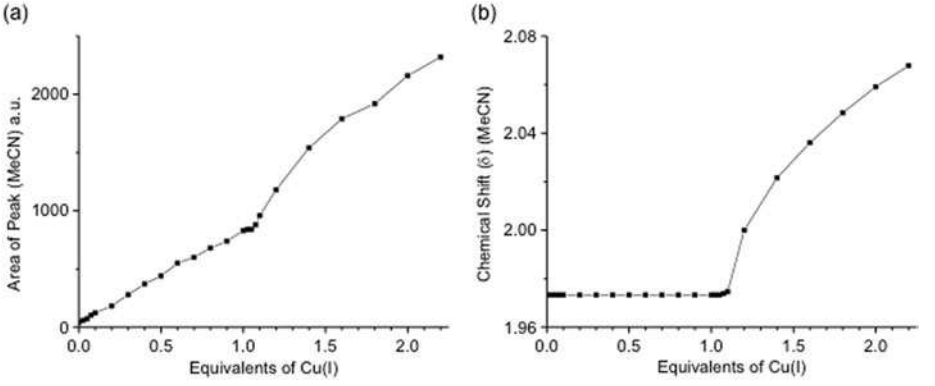

Figure 7. Graphs of the MeCN (a) integrated peak intensity corresponding to the NMR titration and (b) peak position.

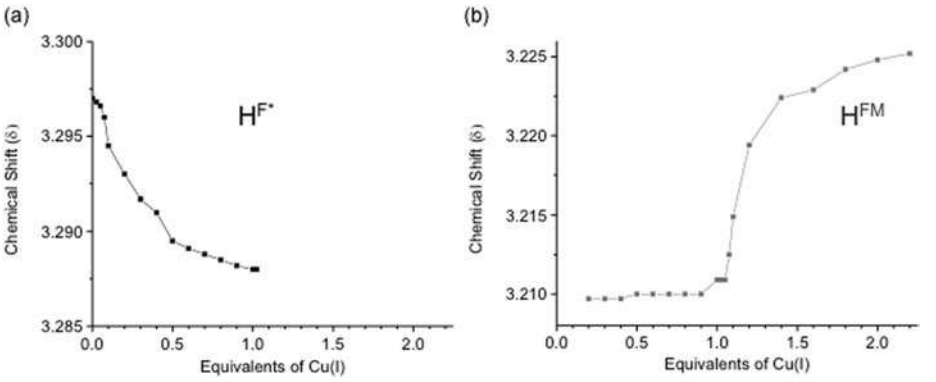

Figure 8. Peak position of (a) proton H^{F*} and (b) proton H^{FM} with equivalents of Cu(I).

which is commonly associated with residual solvent in CD_2Cl_2 (*34*), and holds this position (Figure 7(a)) up to 1 equiv. The downfield migration of the CH_3CN peak starts beyond 1 equiv. and continues to move throughout the titration towards the position observed for a 3-mM solution of $[Cu(MeCN)_4](PF_6)$ in CD_2Cl_2 at ~2.16 ppm (see Supporting Information). This downfield shift reflects the disassembly of the grid, exposing Cu(I) to solution and allowing fast-exchange with labile acetonitrile molecules. During this last half of the titration, the position of the glycol chain's methyl peak, H^{FM} (Figure 8) is seen to migrate downfield during the last half of the titration. Under these conditions, the averaged peak position δ^F_{avg} is the sum of the individual peak positions weighted by their relative abundance. If the grid converted into just one other species, e.g. $[Cu_2\mathbf{L}]^{2+}$, the expression for the average would be δ^F_{avg} $[Cu_4\mathbf{L}_4]\delta_{Cu_4\mathbf{L}_4} + [Cu_2\mathbf{L}]\delta_{Cu_2\mathbf{L}}$, which would result in a *linear* change in peak position under tight binding conditions. The observed peak movement is not linear, consistent with the existence of at least one other intermediate complex. We can conclude from this observation that the grid formed at 1 equiv. disassembles to give two or more complexes during the last half of the titration, i.e. there must exist two phases, IV and V.

To facilitate discussion of the ligand resonances, the change in symmetry and chemical environment of the ligand (Figure 9) within the complexes needs to be accounted for. The free ligand (**L**) has an initial C_2 symmetry that gets broken and reinstated to differing degrees in the complexes. When a single copper ion is bound to a ligand, two sets of inequivalent resonances are expected (Figures 9 and 10). When a ligand is coordinated with two copper ions, it might regain some of its C_2 symmetry. Ultimately, the change from unbound to bound ligand will be accompanied by shifts in peak position reflecting multiple effects: deshielding of hydrogens upon metal coordination and loss of CH ↔ N and production of CH ↔ CH contacts[1] that modify the local environment of hydrogens H^A and H^B (Figure 9). As a consequence of the increasing degree of saturation of the ligands during the first half of the titration, distinct resonances for free ($\mathbf{L}^*$) and complexed ($\mathbf{L}^M$) hydrogens were observed for most resonances (H^B, H^D, H^E and H^F). For example, triazole hydrogen H^{B*} at 8.5 ppm lost intensity (Figure 11) relative to the growth of H^{BM} at 8.8 ppm. Pyridazine protons (H^A), however, appear to show coincidental positions for their L^* and L^M states. Under this schema, it can be seen that peak *intensity* is sensitive to the presence or absence of a bound copper, rather than to the existence of discrete self-assembled species.

Across the titration, there are also small yet diagnostic shifts in the chemical shift positions (Figure 12). Hydrogens H^A, H^F, H^{B*} and H^{BM} all undergo various and non-monotonic positional shifts (± ~ 0.2 ppm) from 0 to

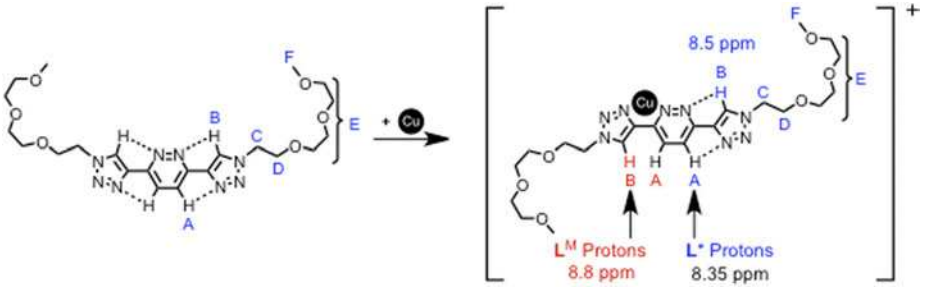

Figure 9. (Colour online) Depiction of inequivalent proton resonances in **L**–Cu complexes.

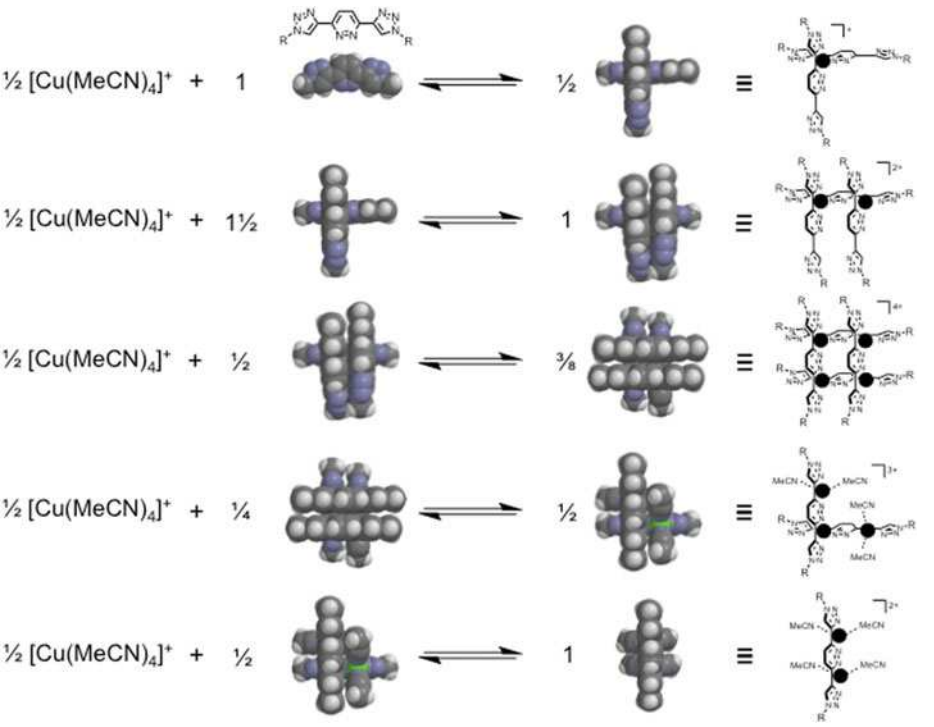

Figure 10. (Colour online) Depiction of complex structures using space-filling models and conventional structure drawings.

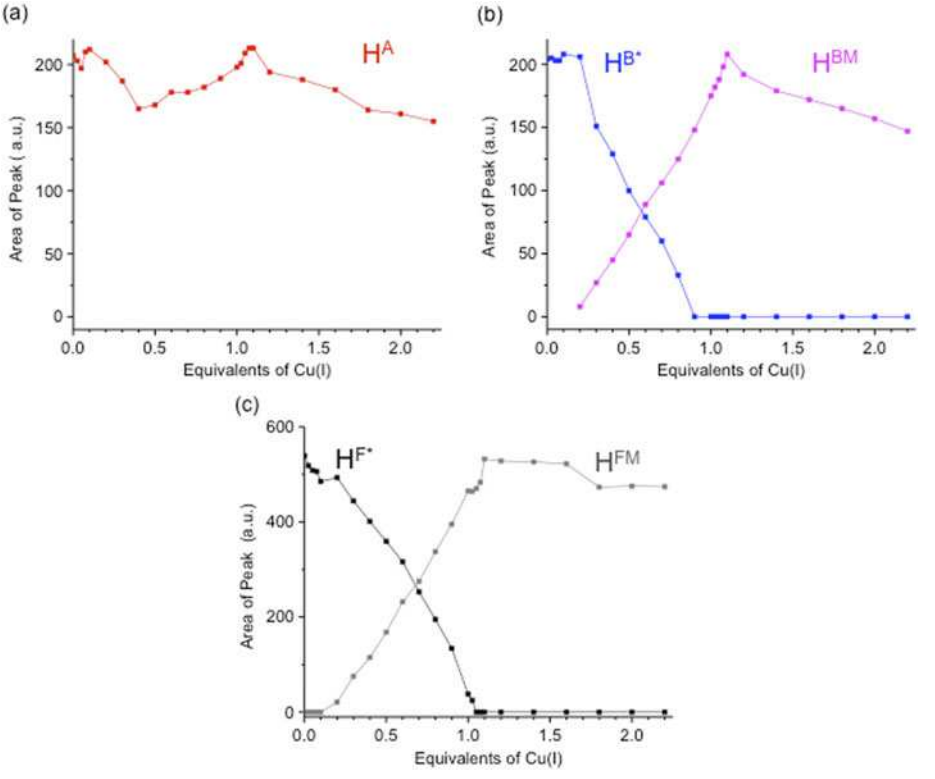

Figure 11. (Colour online) Integrated peak intensities for protons (a) H^{A}, (b) H^{B*} and H^{BM} and (c) H^{F*}/H^{BM} with equivalents of Cu(I).

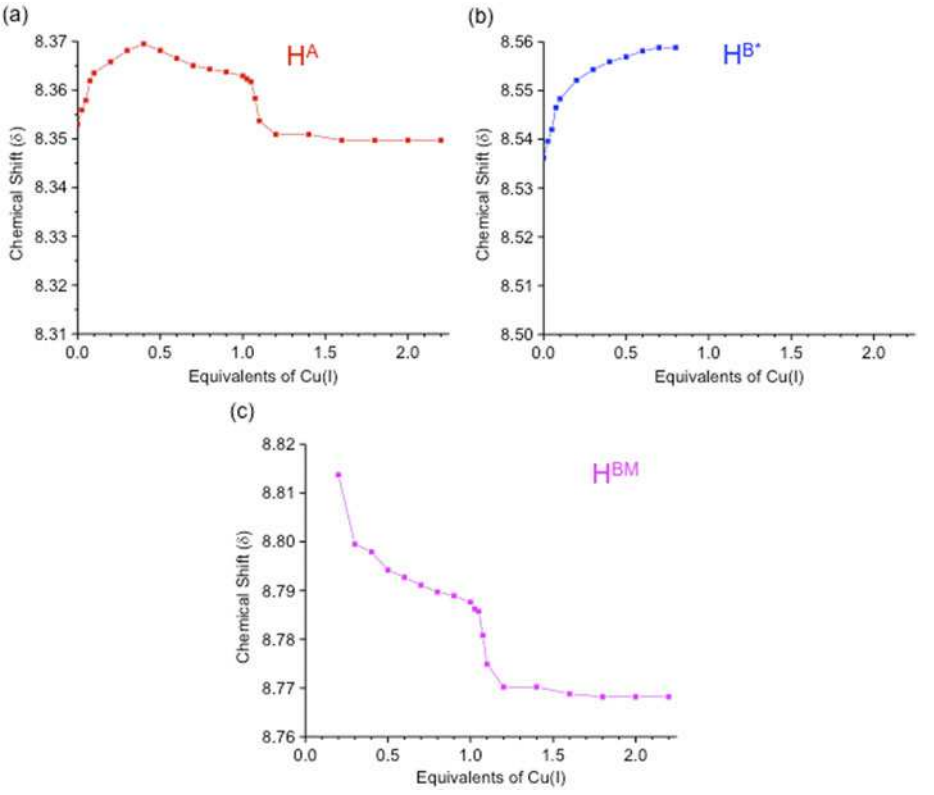

Figure 12. (Colour online) Peak positions of protons (a) H^A, (b) H^{B*} and (c) H^{BM} with equivalents of Cu(I).

1 equiv. of Cu(I). This is consistent with the rich distribution of complexes predicted from the SIVVU™ analysis (Figure 6), underscoring the fact that the assembly process cannot be as simple as $4\mathbf{L} + 4Cu(I)^+ \rightarrow [Cu_4\mathbf{L}_4]^{4+}$.

Using the changes in intensity and position of the key protons (Figures 11 and 12), it is possible to demarcate different phases in the NMR titration. First, peak H^A (Figure 12) shifts downfield (0–0.4 equiv.) and then upfield (0.4–1 equiv.) suggesting there are at least two phases. Second, there is little to no change in the peak intensities from 0 to 0.2 equiv. of Cu(I) for H^{B*} and H^{BM} (Figure 11 (b)) and for H^{F*} and H^{FM} (Figure 11(c)). This behaviour suggests there are at least two phases from 0 to 0.4 equiv. Referring to the simulated speciation curves (Figure 6), these phases can be correlated to the distribution of complexes present in the titration: Phase 1 (0–0.2 equiv.) is dominated by the loss of free ligand to the $[Cu\mathbf{L}_2]^+$ complex. Phase 2 (0.2–0.4 equiv.) shows how the sum of both $[Cu_2\mathbf{L}_3]^{2+}$ and $[Cu\mathbf{L}_2]^+$ in solution start eclipsing the amount of free ligand still present in solution. During the third phase (0.4–1.0 equiv.), we observe the emergence of the grid and the eventual disappearance of all precursor complexes. In total, from 0 to 1.0 equiv. of copper, we observe three intermediate phases (0.0–0.2, 0.2–0.4 and 0.4–1.0) that suggest the presence of four species: the free ligand (0 equiv.), the grid (1.0 equiv.), and two or more intermediates, nominally the $[Cu\mathbf{L}_2]^+$(~0.33 equiv.) and $[Cu_2\mathbf{L}_3]^{2+}$(~0.6 equiv.) complexes seen from the SIVVU™ analysis. These phases can be added to the ones already implicated from the shift in hydrogen H^{FM} (Figure 8) that occurs beyond 1 equiv. to support the speciation curve predicted from SIVVU™ (Figure 6).

While different phases have been seen in the NMR titration, these data do not allow distinct structures to be identified. This gives rise to a quandary: If each complex is in slow exchange, why are no more peaks visible? To rationalise this outcome, consider the small peak migrations observed in protons H^A, H^B and H^F (Figures 8

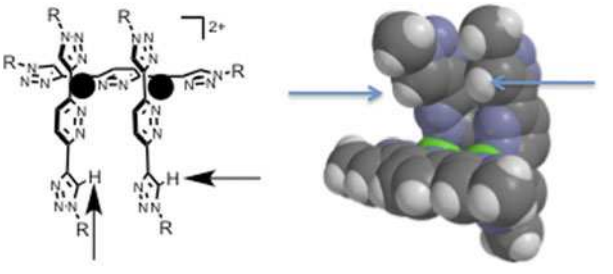

Figure 13. (Colour online) Representation of $[\mathbf{L}_3Cu_2]^{2+}$ in its preferred geometry (molecular modelling) with the inequivalent triazole hydrogens (H^B) marked with arrows.

and 12). These shifts occur both prior to and following the clear slow-exchange from uncomplexed ($\mathbf{L}^{*}$) to complexed ($\mathbf{L}^{M}$) ligands. During all of these small migrations, the peaks are broadened, while at 0, 1 and 2 equiv. they are sharp. Two possible interpretations can be gathered from these observations: first, the broadening results from the co-localisation of nearly identical proton resonances present during the slow exchange processes. Second, the shifts are instead the result of fast-exchange between structural intermediates as the grid is assembled. To distinguish between these interpretations, the ^{1}H NMR titration was carried out at 287 and 370 K with no noticeable change in peak widths at elevated temperatures in deuterated dichloroethane (d_6-DCE). If these five equilibration processes were only undergoing rapid exchange, then they would be expected to show a clear temperature dependence.

The behaviour of the triazole peak H^{B} is exemplary of slow exchange between each complex with coincidentally overlapping peaks. First, we observe a slow exchange process taking place on either side of 0.5 equiv. where the H^{B*} peak at ~ 8.5 ppm loses intensity relative to the growth of the H^{BM} peak at ~ 8.8 ppm. These two peaks are assigned to the uncomplexed and complexed sides of the ligand, respectively (Figure 9). Thus, the triazole protons resonating at ~ 8.5 ppm are a linear combination of the free ligand **L** and the uncomplexed sides of the ligand (Figure 9) that are present in **L**, $[CuL_2]^{+}$ and $[Cu_2L_3]^{2+}$. On account of the fact that these nuclei are on non-coordinated regions of the ligand, it is feasible that they would resonate at similar positions resulting in the appearance of a single broad peak that changes position during the titration. Adding to this complexity, a molecular model of $[Cu_2L_3]^{2+}$ (Figure 13) suggests that two degenerate structures may be accessible with the triazole hydrogens H^{B*} in two slightly different chemical environments, perhaps exchanging rapidly on the NMR timescale. Regarding peak H^{A*} at ~ 8.5 ppm, its position must also arise from the sum of multiple nearly-overlapping peaks undergoing slow exchange on the NMR time scale. On account of the fact that peaks associated with hydrogens H^{A}, H^{B} and H^{F} behave similarly, we believe that exchange between distinct complexes is slow on the NMR timescale.

One final structural observation of novelty is the behaviour of the α-methylene hydrogens, H^{C}. In particular, the splitting of H^{C} from a triplet into two poorly-resolved peaks, potentially a doublet of doublets, provides insight into a possible electronic rearrangement taking place within the triazole. Several studies (*24*, *35*) have previously reported a change in the methylene proton immediately adjacent to the triazole from sharp singlet to either 'broad' or 'multiplet' upon addition of Cu(I). Although the mechanism of this process is unclear, one explanation could be rehybridisation of triazole nitrogen 1-N. Although the aromatic (6π electrons) nature of the triazole ring suggests that all nitrogens would share sp^2 hybridisation, several recent papers (*36*) have shown that conjugation is not extended through to the 1-N in the 1,2,3-triazole ring. Thus, further rehybridisation of the 3-nitrogen from sp^2 to sp^3 would break the planarity of the nitrogen–methylene bond, thus rendering the methylene protons inequivalent. Integration of H^{C} peaks throughout the entirety of the titration shows that the peak intensity does not change, giving support to the hypothesis that the peaks could result from the splitting of the H^{C} triplet into a doublet of doublets. However, to the best of our knowledge, there is no precedent for the loss of planarity of the 3-nitrogen in triazole–Cu(I) complexes.

Table 3. Total free energy values for the formation of each $[Cu_xL_y]$ complex.

Complex formation reaction	ΔG (kJ mol^{-1})
$[Cu(MeCN)_4]^{+} + 2\mathbf{L} \rightleftharpoons [CuL_2]^{+} + 4\,MeCN$	−81
$2[Cu(MeCN)_4]^{+} + 3\mathbf{L} \rightleftharpoons [Cu_2L_3]^{2+} + 8\,MeCN$	−159
$4[Cu(MeCN)_4]^{+} + 4\mathbf{L} \rightleftharpoons [Cu_4L_4]^{4+} + 16\,MeCN$	−294
$3[Cu(MeCN)_4]^{+} + 2\mathbf{L} \rightleftharpoons [Cu_3L_2(MeCN)_4]^{3+} + 8\,MeCN$	−171
$2[Cu(MeCN)_4]^{+} + 1\mathbf{L} \rightleftharpoons [Cu_2L(MeCN)_4]^{2+} + 4\,MeCN$	−93

Evaluation of the energetics of assembly

Clearly, the 2 × 2 grid forms readily in solution and is the dominant (~ 80% at the 10 μM range, ~ 98% at the 3 mM range) complex present at a 1:1 ratio of copper(I) to **L**. However, it is not so dominant as to exclude other species from forming, even at the ideal 1:1 metal:ligand ratio. The free energy values obtained for five chemical equilibria associated with this model are provided in Table 2. Each reaction as written there involves the addition of a half equivalent of a copper cation. This means that exactly one new metal-ligand linkage is established with each of the first three reactions. A linkage constitutes the formation of two copper(I)–nitrogen coordinate bonds, i.e. each bidentate site. As new linkages are formed in the first three steps, the free energy values consistently decrease from approximately −40.5(6) to −30(2) kJ mol^{-1}. This range is consistent with previous ones obtained from the binding of copper(I) ions with similar ligands (*27*). The complete assembly of the grid from the fundamental building blocks of ligand and metal is shown in equilibrium (6).

$$4[Cu(MeCN)_4]^{+} + 4\mathbf{L} \rightleftharpoons [Cu_4L_4]^{4+} + 16\,MeCN. \quad (6)$$

In this reaction as written, eight new metal–ligand linkages are formed and the corresponding 16 acetonitrile

molecules are liberated. The free energy associated with this reaction is $-294\,\mathrm{kJ\,mol^{-1}}$, which is calculated by combining equilibria (1)–(3) from Table 2 in the appropriate ratios. Notably, this value is $30\,\mathrm{kJ\,mol^{-1}}$ greater than eight times the free energy associated with establishing the first linkage ($-40.5(6)\,\mathrm{kJ\,mol^{-1}}$). The difference can be readily accounted for by considering the enthalpy investment required to bring positive cations into close proximity with each other. In the 2×2 grid, there are a total of six pair-wise interactions between Cu(I) cations: four adjacent interactions (3.6 Å) and two more diagonal ones (5.6 and 4.7 Å from the crystal structure). Like the first step Equation (1), the second step as written in Table 2 establishes one new linkage but also brings together two cations adjacent to each other as they bind to the same ligand. Consequently, the free energy associated with this step is only $-37(2)\,\mathrm{kJ\,mol^{-1}}$, which is $3\,\mathrm{kJ\,mol^{-1}}$ less than that of the first. In the third step, again one new linkage is formed, but now multiple Coulombic interactions are established lowering the free energy to just $-31(2)\,\mathrm{kJ\,mol^{-1}}$. Even the size of the second drop-off in free energy ($6\,\mathrm{kJ\,mol^{-1}}$) is roughly twice that of the first drop off. This outcome is expected on account of the fact that only ~37% of the Coulombic interactions are established in the second step and the remaining 63% in the third step.

The free energies of reaction for the formation of the intermediate complexes (Table 3) can also be formulated. The fidelity with which the grid complex is formed can be seen by considering that its formation energy ($-294\,\mathrm{kJ\,mol^{-1}}$), when relative to the species on either side, is considerably larger. For the same reason, the fidelity of formation of any of the other species is quite low, that is, even with the right stoichiometry to form $[\mathrm{Cu}\mathbf{L}_2]^+$, it does not dominate (>90%) the distribution of species in solution. These values compare with those seen for bi-ligand copper(I) complexes of phenanthroline (*37*) for the $[\mathrm{Cu}\mathbf{L}_2]^+$ species which recorded $-68\,\mathrm{kJ\,mol^{-1}}$ in the competitive and high-dielectric MeCN solvent when using 2,9-dimethyl-1,10-phenthroline. This data also pose the question of whether the negative design of the non-grid species can be just as successful as positive design of the grid in enhancing the grid's fidelity at micromolar concentrations.

The drop-offs in free energy from steps 1 to 3 (Table 2) may certainly have additional causes (steric or electronic in nature), but it is difficult to imagine any thermodynamic reasons for counteracting the drop-off. Therefore, $30\,\mathrm{kJ\,mol^{-1}}$ per grid is certainly a safe upper bound for the Coulombic penalty. It is noteworthy that bringing four point charges together at the position of the Cu(I) cations in the crystal structure costs $\sim 2100\,\mathrm{kJ\,mol^{-1}}$ relative to infinite separation. The presence of the counterions and solution must substantially mitigate the charge repulsions.

The titration regime beyond the first equivalent of copper(I) is quite distinct. The final two steps in Table 2 depict the disassembly of the grid upon the further addition of copper(I). The combination of these two steps has a standard free energy of $-80\,\mathrm{kJ/mol}$ per mole of the grid complex.

$$[\mathrm{Cu_4L_4}]^{4+} + 4[\mathrm{Cu(MeCN)_4}]^{+} \rightleftharpoons 4[\mathrm{Cu_2L(MeCN)_4}]^{2+}. \quad (7)$$

It is not surprising that this value is considerably smaller than that associated with the assembly of the grid because even as more copper(I) is added to the solution, no new linkages are formed. Instead only rearrangement occurs. Smaller assemblages ($[\mathrm{Cu_2}\mathbf{L}_3]^{2+}$ and $[\mathrm{Cu_2}\mathbf{L}]^{+}$) begin to dominate as the grid falls apart, ultimately into pairs of Cu(I) cations bound to the same ligand. Noticeably, the ligands remain fully occupied with two cations each. The process does not even involve the loss of all six Coulombic interactions (only the diagonal interactions and two of the four adjacent interactions). While the Coulombic force between the copper(I) cations is certainly a driving force for the disassembly, it only accounts for at most a quarter (about $-20\,\mathrm{kJ\,mol^{-1}}$) of the total free energy associated with disassembly ($-80\,\mathrm{kJ\,mol^{-1}}$). The difference can be explained by considering the effects of entropy. In the disassembly, there are no net linkages established and no acetonitrile molecules released into solution. Because Coulombic forces cannot account for the total free energy, the rearrangements that take place must be predominantly entropy driven. Consequently, disassembly is both entropy and enthalpy driven, with the former being dominant at 298 K.

In the assembly of the grid, the establishment of each new coordination linkage is accompanied by the displacement of two acetonitrile molecules into solution. Therefore, we judge that the assembly process is also entropy driven. The enthalpy drive for assembly is more complicated. Because the new chelate linkages are almost certainly stronger than the solvent coordination, they are likely to contribute to an enthalpy drive. However, it is counteracted by the Coulombic energy penalty of associating positive ions in close proximity, estimated above at $30\,\mathrm{kJ\,mol^{-1}}$ per mole of the grid. It is difficult to ascertain which of these enthalpy effects is more significant from our measurements and analyses. In the case of dications of cobalt forming supramolecular tetrahedra, the assembly was driven only by entropy and apparently hindered by enthalpy (*11*).

Conclusion

Using a variety of supramolecular analysis techniques to take 'snapshots' of solution phase self assembly processes, we have clearly demonstrated the thermodynamic mechanism of the assembly of a $[\mathrm{Cu_4}\mathbf{L}_4]^{4+}$ grid. All five steps, assembly and disassembly, are entropy driven. The disassembly steps are driven primarily by the entropy of

reorganisation of ligands around metal cations ($\sim 60\,kJ\,mol^{-1}$ at 298 K) with the help of a Coulombic enthalpy term ($\sim 20\,kJ\,mol^{-1}$). The entropy that drives the assembly steps is associated with the displacement of acetonitrile ligands into solution. The enthalpy drive of the assembly process could not be definitively ascertained. Any enthalpy associated with the formation of new coordinative linkages will be lowered on account of two effects. First, competition from the Coulombic penalty of bringing positively charged cations into relatively close proximity. Second, a weakening of the donor properties of the second pyridazine nitrogen stemming from through-bond resonance with the first coordinated nitrogen. ESI-MS verified the presence of some complexes, while ^{1}H NMR revealed behaviour in the solution consistent with the modelled assembly mechanism. These results have demonstrated the ability of equilibrium-restricted factor analysis to deconvolute a complicated solution mixture of multiple complexes in equilibrium with each other. By doing so, the assembly process of the two-dimensional supramolecular grid has been ascertained, and thermodynamic and spectral data of various copper(I) complexes have been determined to a high degree of reliability without the need for chemical isolation.

Acknowledgements

This work was supported by the American Chemical Society-Petroleum Research Fund (49503-UR3) and National Science Foundation (CHE-0844441 and CHE-0911527 through the American Recovery and Relief Act).

Note

1. Double arrow (↔) signifies proximity and are not intended to imply the nature of any interactions (attractive or repulsive).

References

(1) (a) Office of Basic Energy Sciences, Office of Science, US. DOE, Version 05-26-06, pmd; (b) Lindsey, J.S. *New J. Chem*. **1991**, *15*, 153–180; (c) Lehn, J.M. *Proc. Natl. Acad. Sci*. **2002**, *99*, 4763–4768.

(2) Aida, T.; Meijer, E.W.; Stupp, S.I. *Science* **2012**, *335*, 813–817.

(3) (a) Alivisatos, A.P.; Barbara, P.F.; Castelman, A.W.; Chang, J.; Dixon, D.A.; Klein, M.L.; McLendon, G.L.; Miller, J.S.; Ratner, M.A.; Rossky, P.J.; Stupp, S.I.; Thompson, M.E. *Adv. Mater.* **1998**, *10*, 1297–1336; (b) Seidel, S.R.; Stang, P.J. *Acc. Chem. Res.* **2002**, *35*, 972–983; (c) Whitesides, G.M.; Grzybowski, B. *Science* **2002**, *295*, 2418–2421; (d) Langner, A.; Tait, S.L.; Lin, N.; Rajadurai, C.; Ruben, M.; Kern, K. *Proc. Natl. Acad. Sci.* **2007**, *104*, 17927–17930; (e) Colson, J.W.; Woll, A.R.; Mukherjee, A.; Levendorf, M.P.; Spitler, E.L.; Shields, V. B.; Spencer, M.G.; Park, J.; Dichtel, W.R. *Science* **2011**, *332*, 228–231; (f) Kissel, P.; Erni, R.; Schweizer, W.B.; Rossell, M.D.; King, B.T.; Bauer, T.; Gotzinger, S.; Schluter, A.D.; Sakamoto, J. *Nat. Chem.* **2012**, *4*, 287–291.

(4) (a) Ito, H.; Kusukawa, T.; Fujita, M. *Chem. Lett.* **2000**, *29*, 598–599; (b) Kuehl, C.J.; Kryschenko, Y.K.; Radhakrishman, U.; Seidel, S.R.; Huang, S.D.; Stang, P.J. *Proc. Natl. Acad. Sci. USA*. **2002**, *99*, 4932–4936; (c) Beltran, L.M.C.; Long, J.R. *Acc. Chem. Res.* **2005**, *28*, 325–334; (d) Lin, C.; Kagan, C.R. *J. Am. Chem. Soc.* **2003**, *125*, 336–337; (e) Hernandez, R.; Tseng, H.-R.; Wong, J.W.; Stoddart, J.F. *J. Am. Chem. Soc.* **2004**, *126*, 3370–3371.

(5) (a) Caulder, D.L.; Powers, R.E.; Aprc, T.N.; Raymond, K. N. *Angew. Chem., Int. Ed.* **1998**, *37*, 1849–1843; (b) Heinrich, J.L.; Berseth, P.A.; Long, J.R. *Chem. Commun.* **1998**, 1231–1232; (c) Kusukawa, T.; Fujita, M. *Angew. Chem., Int. Ed.* **1998**, *37*, 3142–3144; (d) Fujita, M.; Yazaki, J.; Ogura, K. *J. Am. Chem. Soc.* **1990**, *112*, 5645–5647; (e) Stang, P.J.; Persky, N.E.; Mannda, J. *J. Am. Chem. Soc.* **1997**, *119*, 4777–4778.

(6) (a) Parimal, K.; Witlicki, E.H.; Flood, A.H. *Angew. Chem., Int. Ed.* **2010**, *49*, 4628–4632; (b) Share, A.I.; Parimal, K.; Flood, A.H. *J. Am. Chem. Soc.* **2010**, *132*, 1665–1675; (c) McNitt, K.A.; Parimal, K.; Share, A.I.; Fahrenbach, A.C.; Witlicki, E.H.; Pink, M.; Bediako, D.K.; Plaisier, C.L.; Le, N.; Heeringa, L.P.; Vander Griend, D.A.; Flood, A.H. *J. Am. Chem. Soc.* **2009**, *131*, 1305–1313.

(7) Lehn, J.M. *Angew. Chem., Int. Ed. Eng.* **1988**, *27*, 89–112; Lehn, J.M.; *Angew. Chem., Int. Ed. Eng.* **1990**, *29*, 1304–1319.

(8) Olenyuk, B.; Levin, M.D.; Whiteford, J.A.; Shield, J.E.; Stang, P.J. *J. Am. Chem. Soc.* **1999**, *121*, 10434–10435.

(9) Berben, L.A.; Faja, M.C.; Crawford, N.R.M.; Long, J.R. *Inorg. Chem.* **2006**, *45*, 6378–6386.

(10) Young, N.J.; Hay, B.P. *Chem. Commun.* **2013**, *49*, 1354–1379.

(11) Hall, B.R.; Manck, L.E.; Tidmarsh, I.S.; Stephenson, A.; Taylor, B.F.; Blaikie, E.J.; Vander Griend, D.A.; Ward, M.D. *Dalton Trans.* **2011**, *40*, 12132–12145.

(12) Marshall, L.J.; de Mendoza, J. *J. Am. Chem. Soc.* **2013**, *15*, 1548–1551.

(13) (a) Youinou, M-T.; Rahmouni, N.; Fischer, J.; Osborn, J.A. *Angew. Chem., Int. Ed. Engl*. **1992**, *31*, 733–735; (b) Marquis, A.; Kintzinger, J.-P.; Graff, R.; Baxter, P.N.W.; Lehn, J.-M. *Angew. Chem., Int. Ed.* **2002**, *41*, 2760–2764; (c) Dawe, L.N.; Abedin, T.S.M.; Thompson, L.K. *Dalton Trans.* **2008**, *13*, 1661–1665.

(14) Pardo, E.; Cangussu, D.; Lescouëzec, R.; Journaux, Y.; Pasán, J.; Delgado, F.S.; Ruiz-Pérez, C.; Ruiz-Garcia, R.; Cano, J.; Julve, M.; Lloret, F. *Inorg. Chem.* **2009**, *48*, 4661–4673.

(15) (a) Fujita, M.; Sasaki, O.; Watanabe, K.; Ogura, K.; Yamaguchi, K. *New J. Chem.* **1998**, *22*, 189–191; (b) Camara-Campos, A.; Hunter, C.A.; Tomas, S. *Proc. Natl. Acad. Sci.* **2006**, *103*, 3034–3038.

(16) Stojanovic, S.; Turner, D.A.; Share, A.I.; Flood, A.H.; Hadad, C.M.; Badjic, J.D. *Chem. Commun.* **2012**, *48*, 4429–4431.

(17) Fatin-Rouge, N.; Blanc, S.; Pfeil, A.; Rigault, A.; Albrecht-Gary, A.-M.; Lehn, J.-M. *Helv. Chim. Acta* **2001**, *84*, 1694–1711.

(18) Ercolani, G. *J. Am. Chem. Soc.* **2003**, *125*, 16097–16103.

(19) (a) Schweinfurth, D.; Deibel, N.; Weisser, F.; Sarkar, B. *Nachr. Chem.* **2011**, *59*, 937–941; (b) Crowley, J.D.; McMorran, D.A. *Top. Heterocycl. Chem.* **2012**, *28*, 31–84.

(20) (a) Crowley, J.D.; Bandeen, P.H. *Dalton Trans.* **2010**, *39*, 612–623; (b) Gower, M.L.; Crowley, J.D. *Dalton Trans.*

2010, *39*, 2371–2378; (c) Crowley, J.D. Gavey, E.L. *Dalton Trans.* **2010**, *39*, 4035–4037.
(21) Najar, A.M.; Tidmarsh, I.S.; Ward, M.D. *CrystEngComm.* **2010**, *12*, 3642–3650.
(22) Garcia, L.; Maisonneuve, S.; Xie, J.; Guillot, R.; Dorlet, P.; Riviere, E.; Desmadril, M.; Lambert, F.; Policar, C. *Inorg. Chem.* **2010**, *49*, 7282–7288.
(23) Stevenson, K.A.; Melan, C.F.C.; Fleischel, O.; Wang, R.; Petitjean, A. *Cryst. Growth Des.* **2012**, *12*, 5169–5173.
(24) Happ, B.; Pavlov, G.M.; Altuntas, E.; Freibe, C.; Hager, M.D.; Winter, A.; Görls, H.; Günther, W.; Schubert, U.S. *Chem. Asian. J.* **2011**, *6*, 873–880.
(25) (a) Swiegers, G.F.; Malefetse, T.J. *Chem. Rev.* **2000**, *100*, 3483–3537; (b) Ruben, M.; Rojo, J.; Romero-Salguero, F.J.; Uppadine, L.H.; Lehn, J.-M. *Angew. Chem., Int. Ed.* **2004**, *43*, 3644–3662; (c) Chichak, K.S.; Cantrill, S.J.; Pease, A.R.; Chiu, S.-H.; Cave, G.W.V.; Atwood, J.L.; Stoddart, J.F. *Science* **2004**, *304*, 1308–1312; (d) Nitschke, J.R. *Acc. Chem. Res.* **2007**, *40*, 103–112; (e) Ward, M.D. *Chem. Commun.* **2009**, *30*, 4487–4499; (f) Ayme, J.-F.; Beves, J.E.; Leigh, D.A.; McBurney, R.T.; Rissanen, K.; Schultz, D. *Nat. Chem.* **2012**, *4*, 15–20; (g) Chifotides, H. T.; Dunbar, K.R. *Acc. Chem. Res.* **2013**, *46*, 894–906.
(26) Li, Y.; Vander Griend, D.A.; Flood, A.H. *Supramol. Chem.* **2009**, *21*, 111–117.
(27) (a) Bediako, D.K.; DeVries, M.J.; DeJong, N.A.; Heeringa, L.P.; Vander Griend, D.A. Inorg. Chem. **2008**, *47*, 656–662; (b) Flood, A.H.; Li, Y.; Vander Griend, D.A. Supramol. Chem. **2009**, *21*, 111–117; (c) Coluccini, C.; Pasini, D.; Righetti, P. Vander Griend, D.A. Tetrahedron. **2009**, *65*, 10436–10440.
(28) Vander Griend, D.A.; DeVries, M.J. *Sivvu*; Calvin College: Grand Rapids, MI. www.calvin.edu/∼dav4/sivvu 2005.
(29) Caricato, M.; Coluccini, C.; Dondi, D.; Vander Griend, D.A.; Pasini, D. *Org. Biomol. Chem.* **2010**, *8*, 3272–3280.
(30) (a) Caricato, M.; Coluccini, C.; Vander Griend, D.A.; Forni, A.; Pasini, D. *New J. Chem.* **2013**, *37*, 2792–2799; (b) Caricato, M.; Leza, N.J.; Roy, K.; Dondi, D.; Gattuso, G.; Shimizu, L.S.; Vander Griend, D.A.; Pasini, D. *Eur. J. Org. Chem.* **2013**, *27*, 6078–6083.
(31) (a) Malinowski, E.R. *Factor Analysis in Chemistry*, 3rd ed. John Wiley: New York, 2002; (b) Rummel, R.J. *Applied Factor Analysis*, Northwestern University Press: Evanston, IL, 1970.
(32) Hirose, K. *Analytical Methods in Supramolecular Chemistry*; Schalley, C.A., Ed.; Wiley-VCH: Weinheim, 2007.
(33) (a) Poleschak, I.; Kern, J.M.; Sauvage, J.-P. *Chem. Commun.* **2004**, *4*, 474–476; (b) Li, Y.; Huffman, J.C.; Flood, A.H. *Chem. Commun.* **2007**, *26*, 2692–2694; (c) Share, A.I.; Parimal, K.; Flood, A.H. *J. Am. Chem. Soc.* **2010**, *132*, 1665–1675.
(34) The residual solvent peak for MeCN in CD_2Cl_2 is normally observed at 1.95 ppm, see: Gottleib, H.E.; Kotlyar, V.; Nudelman, A. *J. Org. Chem.* **1997**, *62*, 7512–7515. Our observed position was reproduced by the addition of MeCN into a 3.0 mM solution of the ligand in CD_2Cl_2.
(35) Fleischel, O.; Wu, N.; Petitjean, A. *Chem. Commun.* **2010**, *46*, 8454–8456.
(36) (a) van Steenis, D.J.V.C.; David, O.R.P.; van Strijdonck, G.P.F.; van Maarseveen J.H.; Reek, J.N.H. *Chem Commun.* **2005**, *34*, 4333–4335; (b) Juríček, M.; Kouwer, P.H.J.; Rowan, A.E. *Chem Commun.* **2011**, *47*, 8740–8749; (c) Hung, W.-Y.; Tu, G.-M.; Chen, S.-W.; Chi, Y. *J. Mater. Chem.* **2012**, *22*, 5410–5418.
(37) Meyer, M.; Albrecht-Gary, A.-M.; Dietrich-Buchecker, C.O.; Sauvage, J.-P. *Inorg. Chem.* **1999**, *38*, 2279–2287.

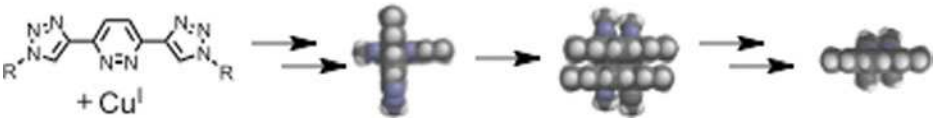

Lauren E. Manck, Christopher R. Benson, Andrew I. Share, Hyunsoo Park, Douglas A. Vander Griend and Amar H. Flood

Self-assembly snapshots of a 2 × 2 copper(I) grid

1–14